Inverse Modeling of GPS Multipath for Snow Depth Estimation—Part I: Formulation and Simulations

Felipe G. Nievinski and Kristine M. Larson

***Abstract*—Snowpacks provide reservoirs of freshwater. The amount stored and how fast it is released by melting are vital information for both scientists and water supply managers. GPS multipath reflectometry (GPS-MR) is a new technique that can be used to measure snow depth. Signal-to-noise ratio data collected by GPS instruments exhibit peaks and troughs as coherent direct and reflected signals go in and out of phase. These interference fringes are used to retrieve the unknown land surface characteristics. In this two-part contribution, a forward/inverse approach is offered for GPS-MR of snow depth. Part I starts with the physically based forward model utilized to simulate the coupling of the surface and antenna responses. A statistically rigorous inverse model is presented and employed to retrieve parameter corrections responsible for observation residuals. The unknown snow characteristics are parameterized, the observation/parameter sensitivity is illustrated, the inversion performance is assessed in terms of its precision and its accuracy, and the dependence of model results on the satellite direction is quantified. The latter serves to indicate the sensing footprint of the reflection.**

***Index Terms*—Artificial satellites, electromagnetic reflection, global positioning system, interferometers, multipath channels, radar remote sensing.**

I. Introduction

SNOWPACKS provide reservoirs of freshwater, storing solid precipitation and delaying runoff [1]. One sixth of the world population depends on this resource [2]. Both scientists and water supply managers need to know how much freshwater is stored in snowpack and how fast it is being released as a result of melting [3].

Snow monitoring from space is currently under investigation by both NASA (Snow and Cold Land Processes mission) and ESA (Cold Regions Hydrology High-Resolution Observatory). Greatly complementary to such spaceborne sensors are automated ground-based methods; the latter not only serves as essential independent validation and calibration for the former but are also valuable for climate studies and flood/drought monitoring on their own. It is desirable for such estimates to be provided at an intermediary scale, between point-like *in situ* samples and wider area pixels.

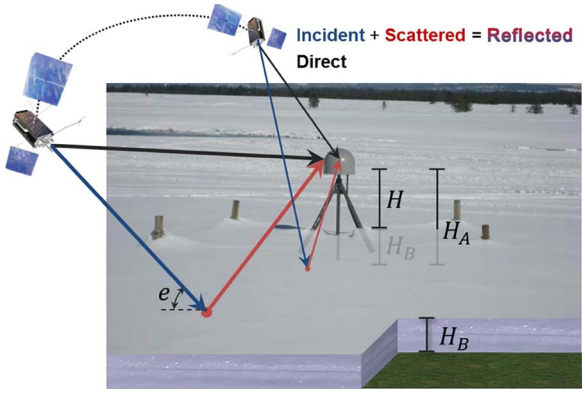

Fig. 1. Standard geodetic receiver installation. The antenna is protected by a hemispherical radome. The monument (tripod structure) is ∼2 m above the ground. GPS satellites rise and set in ascending and descending sky tracks, multiple times per day. The specular reflection point migrates radially away from the receiver for decreasing satellite elevation angle. The total reflector height is made up an *a priori* value and an unknown bias driven by thickness of the snow layer.

In the last decade, GPS multipath reflectometry (GPS-MR) has been proposed for monitoring snow. This method tracks direct GPS signals, those that travel directly to an antenna, that have interfered with a coherently reflected signal, turning the GPS unit into an interferometer (Fig. 1). Although GPS-MR is a subset of GPS reflectometry (GPS-R), we do not consider GPS-R incoherent sensing and/or separate tracking of direct and reflected signals as well as targets other than snow. In [4], a theory for GPS reflections off snow in layered media was presented and compared with observations; more recently, [5] has evaluated the possibility of retrieving snow density in addition to snow depth. In [6], a demonstration was made of subsurface sensing in dry snow, based on complex-valued (power and phase) tracking waveforms over varying propagation delays. The spectral analysis of a stack of such delay waveforms over varying angles of incidence was found in agreement with snow layering. In [7], a linearly polarized antenna was employed, resulting in an interference pattern exhibiting notches arising from reflections at each of the air/snow/ground interfaces. Independent *in situ* snow depth measurements were necessary to constrain the inversion problem and retrieve the correct solution. In [8], a retrieval method based on dual-frequency linear combination of carrier-phase measurements was proposed. In [9], several pertinent simulations were performed. Finally, in [10]–[12], a new kind of GPS-MR method was introduced and developed. It is based on signal-to-noise ratio

Manuscript received June 16, 2013; revised November 13, 2013; accepted December 12, 2013. Date of publication January 31, 2014; date of current version May 22, 2014. This work was supported by the National Science Foundation (NSF) (EAR 0948957 and AGS 0935725), by the National Aeronautics and Space Administration (NASA) (NNX12AK21G), and by a CU interdisciplinary seed grant. Dr. Nievinski has been supported by a Capes/Fulbright Graduate Student Fellowship (1834/07-0) and a NASA Earth System Science Research Fellowship (NNX11AL50H).

F. G. Nievinski is with the Departamento de Cartografia, Universidade Estadual Paulista "Júlio de Mesquita Filho," Presidente Prudente, SP 19060-900 Brazil (e-mail: fgnievinski@gmail.com).

K. M. Larson is with the Department of Aerospace Engineering Sciences, University of Colorado, Boulder, CO 80309 USA (e-mail: kristinem.larson@gmail.com).

Color versions of one or more of the figures in this paper are available online at http://ieeexplore.ieee.org.

Digital Object Identifier 10.1109/TGRS.2013.2297681

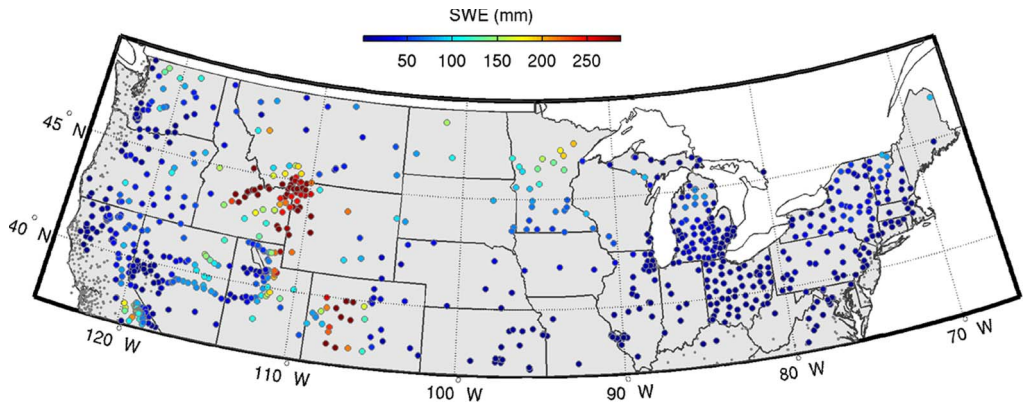

Fig. 2. Continuously operating GPS sites in the contiguous U.S.—both PBO (http://pboweb.unavco.org/) and CORS (http://www.ngs.noaa.gov/CORS/) networks. Color values are climatic annual snow water equivalent (SWE) [20]; values are clipped at 97.5% for greater color discrimination; GPS sites with negligible SWE (<1 mm) are shown as gray smaller dots.

(SNR) measurements collected by existing GPS base stations that employ geodetic-quality receivers and antennas (Fig. 2).

Here, we offer a detailed and full exploration of the SNR-based GPS-MR technique as applied to snow sensing and using geodetic instruments. This forward/inverse approach for GPS-MR is new in that it capitalizes on known information about the antenna response and the physics of surface scattering to aid in retrieving the unknown snow conditions in the site surroundings (Fig. 3). It is a more rigorous retrieval algorithm, agreeing to first order with the simpler original methodology, which is retained here for the inversion bootstrapping (see Section III-C). This contribution has two parts. This paper describes the retrieval algorithm. Part II of this paper [13] will provide validation at three representative sites for 1–3 years. Section II presents the physically based forward model utilized to simulate the coupling of the surface and antenna responses. Then, we present the statistically rigorous inverse model employed to retrieve parameter corrections responsible for observation residuals. Section III explains how the unknown snow characteristics were parameterized in terms of a few biases embedded in the forward model. In Section IV, we illustrate the observation/parameter sensitivity. Section V assesses the inversion performance in terms of errors (retrievals minus truth) and their uncertainty ("errorbars"). We end by quantifying the dependence of model results on the satellite direction in Section VI.

II. Physical Forward Model Review

This section presents a short review of the forward model illustrated extensively elsewhere [14]. SNR observations are formulated as $\mathrm{SNR} = P_\mathrm{s}/P_\mathrm{n}$. In the denominator, we have the noise power P_n, here taken as a constant, based on nominal values for the noise power spectral density and the noise bandwidth. The numerator is composite signal power

$$P_\mathrm{s} = P_\mathrm{s}^\mathrm{I} + P_\mathrm{s}^\mathrm{C}. \tag{1}$$

Its incoherent component is the sum of the respective direct and reflected powers (although direct incoherent power is negligible)

$$P_\mathrm{s}^\mathrm{I} = P_\mathrm{d}^\mathrm{I} + P_\mathrm{r}^\mathrm{I} \approx P_\mathrm{r}^\mathrm{I}. \tag{2}$$

In contrast, the coherent composite signal power $P_\mathrm{s}^\mathrm{C} = |\langle V_\mathrm{s}\rangle|^2$ follows from the complex sum $\langle V_\mathrm{s}\rangle = \langle V_\mathrm{d}\rangle + \langle V_r\rangle$ of direct and reflection average voltages (not to be confused with the EM propagating fields, which neglect the receiving antenna response and also the receiver tracking process)

$$P_\mathrm{s}^\mathrm{C} = P_\mathrm{d}^\mathrm{C} + P_\mathrm{r}^\mathrm{C} + 2\sqrt{P_\mathrm{d}^\mathrm{C}}\sqrt{P_\mathrm{r}^\mathrm{C}}\cos\phi_\mathrm{i}. \tag{3}$$

It is expressed in terms of the coherent direct $P_\mathrm{d}^\mathrm{C} = |\langle V_\mathrm{d}\rangle|^2$ and reflected $P_\mathrm{r}^\mathrm{C} = |\langle V_r\rangle|^2$ powers, as well as the interferometric phase

$$\phi_\mathrm{i} = \phi_\mathrm{r} - \phi_\mathrm{d} \tag{4}$$

which amounts to the reflection excess phase with respect to the direct signal. An equivalent formulation $\langle V_\mathrm{s}\rangle = \langle V_\mathrm{d}\rangle \cdot (1 + \langle V_\mathrm{i}\rangle)$ involving only interferometric quantities $\langle V_\mathrm{i}\rangle = \langle V_\mathrm{r}\rangle/\langle V_\mathrm{d}\rangle = \sqrt{P_\mathrm{i}^\mathrm{C}}\exp(\iota\phi_\mathrm{i})$, with the imaginary unity denoted $\iota = \sqrt{-1}$, reads [14]

$$P_\mathrm{s}^\mathrm{C} = P_\mathrm{d}^\mathrm{C}\left(1 + P_\mathrm{i}^\mathrm{C} + 2\sqrt{P_\mathrm{i}^\mathrm{C}}\cos\phi_\mathrm{i}\right). \tag{5}$$

We decompose observations $\mathrm{SNR} = \mathrm{tSNR} + \mathrm{dSNR}$ into a trend

$$\mathrm{tSNR} = (P_\mathrm{d} + P_\mathrm{r})/P_\mathrm{n} = \left(P_\mathrm{d}^\mathrm{C} + P_\mathrm{r}^\mathrm{C} + P_\mathrm{s}^\mathrm{I}\right)/P_\mathrm{n} \tag{6}$$

over which interference fringes are superimposed

$$\mathrm{dSNR} = 2\sqrt{P_\mathrm{d}^\mathrm{C}}\sqrt{P_\mathrm{r}^\mathrm{C}}P_\mathrm{n}^{-1}\cos\phi_\mathrm{i}. \tag{7}$$

From now on, we neglect incoherent power P_s^I—which only impacts tSNR and not dSNR—and drop the coherent power superscript for brevity.

The direct or line-of-sight power is formulated as

$$P_\mathrm{d} = P_\mathrm{d}^\mathrm{R} G_\mathrm{d}^\mathrm{R} \tag{8}$$

where P_d^R is the direction-dependent right-hand circularly polarized (RHCP) power component incident on an isotropic antenna, as specified in the GPS interface [GPSD-USAF, 2011]; the same document specifies the left-handed circularly polarized (LHCP) component to be negligible. The direct antenna gain G_d^R is obtained by evaluating the antenna pattern at the satellite direction and at RHCP polarization. For several

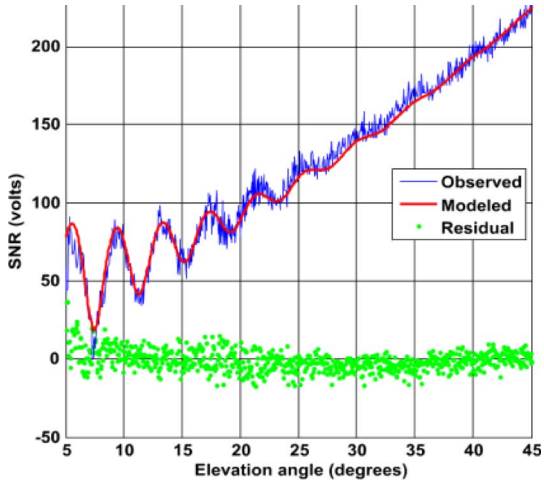

Fig. 3. Inversion results (red trace) over measurements (blue) for a single GPS track and corresponding residuals (green dots). The deep fades are a consequence of the destructive interference between direct and reflected signals. Residuals, originally zero-centered, have been displaced vertically for clarity. SNR units are normalized by an arbitrary constant for clarity.

commonly used antennas, the full pattern is made available by the antenna manufacturing company.

The reflection power

$$P_{\mathrm{r}} = P_{\mathrm{d}}^{\mathrm{R}} |X|^2 S^2 \tag{9}$$

is defined starting with the same incident isotropic power $P_{\mathrm{d}}^{\mathrm{R}}$ as in the direct power P_{d}. It ends with a coherent power attenuation factor [15], [16]

$$S^2 = \exp(-k^2 s^2 \cos^2 \theta) \tag{10}$$

where θ is the angle of incidence (with respect to the surface normal), $k = 2\pi/\lambda$ is the wavenumber, and $\lambda = 24.4$ cm is the carrier wavelength for the civilian GPS signal on the L2 frequency (L2C). This polarization-independent factor accounts only for small-scale residual height above and below a large-scale trend surface. The former/latter results from high-/low-pass filtering the actual surface heights using the first Fresnel zone as a convolution kernel, roughly speaking. Small-scale roughness is parameterized in terms of an effective surface standard deviation s (in meters); its scattering response is modeled based on the theories of random surfaces, except that the theoretical ensemble average is replaced by a spatial average in measurements. Large-scale deterministic undulations could be modeled via, for example, ray-tracing and are outside the scope of this paper; its impact on snow depth is canceled to first order by removing bare-ground reflector heights.

At the core of P_{r}, we have coupled surface/antenna reflection coefficients $X = X^{\mathrm{R}} + X^{\mathrm{L}}$ defined here as

$$X^{\mathrm{R}} = R^{\mathrm{S}} \sqrt{G_{\mathrm{r}}^{\mathrm{R}}} \exp\left(\iota \Phi_{\mathrm{r}}^{\mathrm{R}}\right) \tag{11}$$

$$X^{\mathrm{L}} = R^{\mathrm{X}} \sqrt{G_{\mathrm{r}}^{\mathrm{L}}} \exp\left(\iota \Phi_{\mathrm{r}}^{\mathrm{L}}\right) \tag{12}$$

producing, respectively, RHCP and LHCP fields (under the assumption of RHCP incident field—see [14] for generalizations). The antenna response includes the power gain G and the phase Φ patterns, evaluated at the reflection direction and separately for each polarization. The surface response is represented by the complex-valued Fresnel coefficients R^{X}, R^{S} for cross- and same-sense circular polarization, respectively. The medium is assumed to be homogeneous (i.e., a semi-infinite half-space). Material models provide the complex permittivity which drives the Fresnel coefficients. We employ the permittivity value derived in [4], obtained by evaluating the snow permittivity model of [17] at nominal snow density and temperature.

The interferometric phase reads

$$\phi_{\mathrm{i}} = \phi_X + \phi_{\mathrm{I}} - \Phi_{\mathrm{d}}^{\mathrm{R}}. \tag{13}$$

The first term $\phi_X = \arg(X)$ accounts for the surface and antenna properties of the reflection, as in the previous discussion. The last one $\Phi_{\mathrm{d}}^{\mathrm{R}}$ is the direct phase contribution, which amounts to only the RHCP antenna phase center variation evaluated at the satellite direction. The majority of the components present in the direct RHCP phase ϕ_{d} (such as receiver and satellite clock states, the bulk of atmospheric propagation delays, etc.) is also present in the reflection phase ϕ_{r}, so they cancel out in forming the difference $\phi_{\mathrm{i}} = \phi_{\mathrm{r}} - \phi_{\mathrm{d}}$.

At the core of the interferometric phase ϕ_{i}, we have the geometric component $\phi_{\mathrm{I}} = k\tau_{\mathrm{i}}$, the product of the wavenumber k (in radians per meter), and the interferometric propagation delay τ_{i} (in meters). Assuming a locally horizontal surface, the latter is simply [18]

$$\tau_{\mathrm{i}} = 2H_A \sin e \tag{14}$$

in terms of the satellite elevation angle e and an *a priori* reflector height H_A. Snow depth will be measured in terms of changes in reflector height.

The physical forward model, based only on *a priori* information, can be summarized as

$$\mathrm{SNR} = P_{\mathrm{d}}(1 + P_{\mathrm{i}} + 2\sqrt{P_{\mathrm{i}}} \cos \phi_{\mathrm{i}})/P_{\mathrm{n}} + P_{\mathrm{s}}^{\mathrm{I}}/P_{\mathrm{n}} \tag{15}$$

where interferometric power and phase are, respectively

$$P_{\mathrm{i}} = |XS|^2 / G_{\mathrm{d}}^{\mathrm{R}} \tag{16}$$

$$\phi_{\mathrm{i}} = \phi_X + 4\pi\lambda^{-1} H_A \sin e - \phi_{\mathrm{d}}^{\mathrm{R}}. \tag{17}$$

In all of these terms, the CDMA modulation impressed on the carrier wave can be safely neglected, given the small interferometric delay and Doppler at grazing incidence, stationary surface/receiver conditions, and short antenna installations [14].

III. Parameterization of Unknowns

There are errors in the nominal values assumed for the physical parameters of the model (permittivity, surface roughness, reflector height, etc.). Ideally, we would estimate separate corrections for each one, but unfortunately, many are linearly dependent or nearly so. Because of this dependence, we have kept physical parameters fixed to their optimal *a priori* values and have estimated a few biases. Each bias is an amalgamation of corrections for different physical effects. In a later stage, we rely on multiple independent bias estimates (e.g., successive days) to try and separate some of the physical sources.

A. Biases

The original noise power P_{n} will be augmented as P_{n}/K to include a bias K accounting for imperfections in the nominal trend of direct power versus elevation angle $(P_{\mathrm{d}}^{\mathrm{R}})$—including unanticipated attenuations along the line of sight, such as foliage, precipitation, etc.—and also in the nominal values of all other linearly dependent parameters, mainly antenna gain $G_{\mathrm{d}}^{\mathrm{R}}$ (direction dependent) and the nominal noise power P_{n} (direction independent; it is time dependent). The noise power bias K must be nonnegative, yet the optimization is performed over the real numbers, so we handle this bias expressed in decibels $(K_{\mathrm{dB}} = 10\log_{10} K)$. Furthermore, we expand it as a polynomial in terms of powers of sine of elevation angle $\sin e$

$$K_{\mathrm{dB}} = \sum_{j=0,1,\ldots} K_{\mathrm{dB}}^{(j)} \sin^j e = K_{\mathrm{dB}}^{(0)} + K_{\mathrm{dB}}^{(1)} \sin e + K_{\mathrm{dB}}^{(2)} \sin^2 e + \cdots. \tag{18}$$

We also introduce an elevation angle dependent complex bias $B = |B| \exp(\iota\phi_B)$ as a correction for imperfections in the reflection model; it will compensate for both errors of commission (e.g., surface roughness that, although accounted for, is over- or underestimated) and errors of omission (e.g., volumetric inhomogeneities that are completely ignored). Reflection power gets updated as $P_{\mathrm{r}}/|B|^2$ and interferometric phase as $\phi_{\mathrm{i}} - \phi_B$. Similar as that for the noise power bias K, we define the polynomials in $\sin e$ for the reflection power bias $B_{\mathrm{dB}} = \sum_{j=0,1,\ldots} B_{\mathrm{dB}}^{(j)} \sin^j e$ and for the reflection phase bias $\phi_B = \sum_{j=0,1,\ldots} \phi_B^{(j)} \sin^j e$.

We single out the first two phase bias coefficients. The constant term $\phi_B^{(0)} = \varphi_B$ is a phase shift accounting for errors in the antenna phase pattern Φ, in the medium composition, surface tilting, etc. The linear phase coefficient $\phi_B^{(1)}$ gets recast as an equivalent horizontal-surface reflector height

$$H_B = \phi_B^{(1)} \lambda/(4\pi). \tag{19}$$

It accounts for errors in the *a priori* value for the reflector height, including the unknown thickness of a snow layer deposited over the ground and a tilting in the underlying ground (yielding a positive topographical height bias downhill and negative uphill). The full phase bias function is rewritten as

$$\phi_B = \varphi_B + 4\pi\lambda^{-1} H_B \sin e + \phi_B^{\wedge} \tag{20}$$

where the phase remainder $\phi_B^{\wedge} = \sum_{j=2,3,\ldots} \phi_B^{(j)} \sin^j e$ contains higher order terms $j = 2, 3$.

The forward model, including biases, can be summarized as follows—cf., (4), (6), and (7):

$$\mathrm{SNR} = (1 + P_{\mathrm{i}} + 2\sqrt{P_{\mathrm{i}}} \cos\phi_{\mathrm{i}}) P_{\mathrm{d}} K/P_{\mathrm{n}} + P_{\mathrm{s}}^{\mathrm{I}}/P_{\mathrm{n}} \tag{21}$$

where interferometric power and phase are, respectively

$$P_{\mathrm{i}} = |XS/B|^2 / G_{\mathrm{d}}^{\mathrm{R}} \tag{22}$$

$$\phi_{\mathrm{i}} = \phi_X + 4\pi\lambda^{-1} H \sin e - \varphi_B - \phi_B^{\wedge} - \Phi_{\mathrm{d}}^{\mathrm{R}}. \tag{23}$$

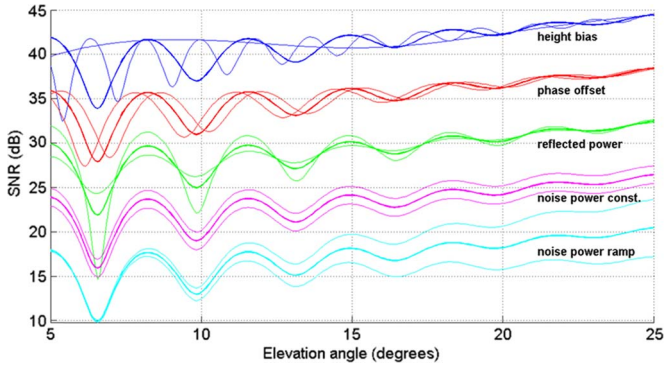

Fig. 4. Effect of each parameter on SNR observations; curves are displaced vertically (6 dB) for clarity.

The total reflector height $H = H_A - H_B$ (*a priori* value minus unknown bias) is to be interpreted as an effective value that best fits measurements, which includes snow and other components.

B. Observation Partitioning and Parameter Update Rate

For many GPS sites, SNR observations are recorded at 1-s time intervals. We decimated this data stream to 10 s. Satellite azimuth and elevation angle are calculated from the broadcast ephemerides. Elevation angle is the one variable over which the model varies the most: reflection coefficients, surface roughness, interferometric propagation delay, and antenna gain pattern. Therefore, it is desirable to maximize the range of observed elevation angles per track if the various parameters being jointly estimated are to be resolved without ambiguity. Azimuth, on the other hand, offers little opportunity for such a decorrelation, besides introducing the risk of conflating distinct scattering conditions (e.g., presence versus absence of trees, varying snow depth due to different orientation to the Sun, etc.); therefore, we wish to minimize the azimuth range per track.

Each satellite track is inverted independently. A track is defined by partitioning the data by individual satellite and then into ascending and descending portions, splitting the period between the satellite's rise and set, at the near-zenith culmination. Each satellite track has a duration of ∼1–2 h. This configuration normally offers a sufficient range of elevation angles, unless the satellite reaches culmination too low in the sky $(\lesssim 20^\circ)$, in which case the track is discarded. In seeking a balance between under- and overfitting, between insufficient and excessive numbers of parameters, we estimate the following unknown parameters:

$$X = \left[H_B, \varphi_B, B_{\mathrm{dB}}^{(0)}, B_{\mathrm{dB}}^{(1)}, B_{\mathrm{dB}}^{(2)}, K_{\mathrm{dB}}^{(0)}, K_{\mathrm{dB}}^{(1)}, K_{\mathrm{dB}}^{(2)}\right]^{\mathrm{T}}. \tag{24}$$

Fig. 4 shows the effect of the constant and linear biases on the SNR observations. Reflector height bias H_B changes the number of oscillations; phase shift φ_B displaces the oscillations along the horizontal axis; reflection power $B_{\mathrm{dB}}^{(0)}$ affects the depth of fades; zeroth-order noise power $K_{\mathrm{dB}}^{(0)}$ shifts the observations up or down as a whole; and first-order noise power $K_{\mathrm{dB}}^{(1)}$ tilts the SNR curve. A good parameterization yields observation sensitivity curves as unique as possible for each parameter, as shown in the following discussion.

C. Bootstrapping Parameter Priors

Biases and SNR observations are involved nonlinearly through the forward model. Therefore, there is the need for a preliminary global optimization, without which the subsequent final local optimization will not necessarily converge to the optimal solution.

SNR observations would trace out a perfect sinusoid curve in the case of an antenna with isotropic gain and spherical phase pattern, surrounded by a smooth, horizontal, and infinite surface (free of small-scale roughness, large-scale undulations, and edges), made of perfectly electrically conducting material, and illuminated by constant incident power. Thus, in such an idealized case, taking $4\pi\lambda^{-1}\sin e$ as the independent variable, SNR could be described exactly by constant reflector height, phase shift, amplitude, and mean value.

As the measurement conditions become more complicated, the SNR data start to deviate from a pure sinusoid. However, a polynomial/spectral decomposition is often adequate for bootstrapping purposes. We start simulating a trend tSNR$'$ free of interference fringes by artificially forcing $\phi_{\rm i} = 90^\circ$ so that $\cos\phi_{\rm i}$ is nullified. The ratio between measured and simulated observations rSNR $=$ SNR/tSNR$'$ provides trend residuals which are fit by a low-order polynomial. The resulting noise power bias $K = 10^{K_{\rm dB}/10}$ is subsequently employed to update the trend simulation tSNR$'$. Next, we detrend measurements dSNR $=$ SNR $-$ tSNR$'$ as well as simulations dSNR$'$ $=$ SNR$'$ $-$ tSNR$'$, which leaves just the respective fringes. We then fit a sinusoid separately to each dSNR and dSNR$'$; it is found by seeking the peak amplitude in a Lomb–Scargle periodogram. This step yields two sets of reflector height, phase shift, and amplitude: H, φ, and A for measurements and H', φ', and A' for simulations. Finally, we subtract the simulated results from the measured ones

$$H_B = H' - H \tag{25}$$
$$\varphi_B = \varphi' - \varphi \tag{26}$$
$$|B| = A/A'. \tag{27}$$

This cancels out the known effects; for example, the normalization $|B| = A/A'$ is crucial if reflection power estimates are to be independent of the particular antenna gain utilized. The resulting approximate values for the unknown biases $(H_B, \varphi_B, |B|)$ are utilized as initial values for the zeroth-order polynomial coefficients, e.g., $B^{(0)}_{\rm dB} = \log_{10}(20|B|)$; higher order parameters are initialized as zero. These possibly coarse estimates will be refined by the statistical optimization now that the inversion is bootstrapped.

IV. Statistical Inverse Model Formulation

Based on the preliminary values for the unknown parameter vector X and other known (or assumed) values, we run the forward model to obtain simulated observations $f(X)$. We form prefit residuals $y = Y - f(X)$ comparing $f(X)$ to SNR measurements $Y = [\text{SNR}_1, \text{SNR}_2, \ldots]^{\rm T}$ collected at varying satellite elevation angles (separately for each track). Residuals serve to retrieve parameter corrections

$$\widehat{x} = C_{\widehat{x}} J^{\rm T} C_y^{-1} y \tag{28}$$

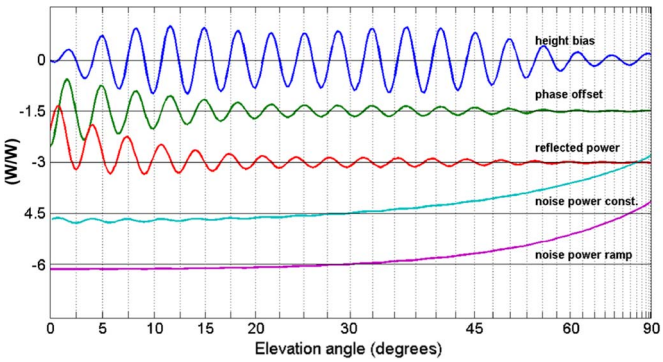

Fig. 5. Sensitivity of observations (in original units of watts per watt) to changes in each bias; curves are scaled and displaced vertically (1.5 W/W) for clarity.

such that the squared sum $\widehat{y}^{\rm T}\widehat{y}$ of postfit residuals $\widehat{y} = Y - f(X - \widehat{x})$ is minimized. This nonlinear least squares problem is solved iteratively. The impact of matrices J and C_y is discussed in the following.

A. Functional Model

The Jacobian matrix J is the main component in the inversion. It represents the sensitivity of observations to parameter changes

$$J(i,j) = \partial Y_i / \partial X_j \tag{29}$$

where the partial derivative is defined elementwise. Instead of deriving analytical expressions, we evaluate them numerically via finite differencing. Fig. 5 shows each column of the Jacobian matrix as a line trace. The sensitivities with respect to reflector height and phase shift are aligned with each other and exhibit, respectively, an increasing and decreasing magnitude over increasing elevation angle. If SNR observations were a perfect sinusoid, the two sensitivities would be mirrored copies of each other, coinciding at the central elevation angle. The longer the track, the more distinct the two sensitivity curves are. Conversely, the shorter the track, the more difficult it is to distinguish reflector height and phase-shift effects. Consequently, their parameter estimates will exhibit significant correlation, which, in turn, will increase the reflector height uncertainty. Were it possible to account for phase shift in the forward model and exclude or at least tightly constrain it in the inverse model, reflector height precision would be greatly improved. Conversely, constraining reflector height would improve the precision of phase-shift estimates.

The sensitivity with respect to reflected power bias—essentially a scaled version of the detrended SNR observations—is in phase quadrature with that of reflector height and phase shift. This orthogonality implies that the former can be decorrelated well from the latter two parameters. This is not to say that reflection power has no impact on the reflector height uncertainty. The sensitivity of observations with respect to reflector height depends not only on reflector height itself but potentially also on all other parameters. Indeed, if the reflection power becomes too small, simulated observations lose sensitivity to reflector height: $\lim_{B_{\rm dB}\to-\infty} \partial Y/\partial H_B = 0$.

This may be caused by a genuine physical effect, as in the case of random surface roughness; other times, it is an undesirable numerical artifact arising from an inadequate optimization (see the following discussion for ways to mitigate this via the stochastic model).

Finally, the sensitivities with respect to noise power would, in principle, be simply polynomial bases, i.e., zeroth and first-order powers of sine of elevation angle. However, these sensitivities fail to exhibit a purely constant or linear behavior. That is because the polynomial is defined in decibels (necessary to guarantee nonnegative power). In contrast, we take observations in watts per watt because these are the units in which fringes are supposed to most resemble a sinusoid. Finally, the estimation of noise power bias only affects the reflector height uncertainty for very small total reflector heights; in this case, both sensitivities will exhibit large-period oscillations, resembling a low-order polynomial. Thus, the impact arises from the near colinearity between the two parameters and not from the noise power sensitivity alone.

B. Stochastic Model

We need to specify the uncertainty and correlation expected in residuals y. Their prior covariance matrix C_y modifies the objective function being minimized. It cannot be simply a multiple of the identity matrix because SNR measurements are reported in decibels, which yields a logarithm scaling in watts per watt. Starting with a homogeneous residual variance in decibels $\sigma^2_{y_{i\mathrm{dB}}}$, we obtain heterogeneous variances via the delta method

$$\sigma^2_{y_i} = \sigma^2_{y_{i\mathrm{dB}}} \left(\partial Y_i / \partial Y_{i\mathrm{dB}}\right)^2 \tag{30}$$

so variances are scaled in proportion to the decibel-to-power transformation itself

$$\frac{\partial Y_i}{\partial Y_{i\mathrm{dB}}} = \mathrm{SNR}_i \ln(10)/10 \tag{31}$$

where $\mathrm{SNR}_i = 10^{\mathrm{SNR}_{i\mathrm{dB}}/10}$. We form a diagonal residual covariance matrix $C_y = \mathrm{Diag}(\Sigma_y)$ given the vector $\Sigma_y = [\sigma^2_{y_1}, \sigma^2_{y_2}, \ldots]^{\mathrm{T}}$ of transformed variances over each ith satellite direction. Such a data transformation is used to make the observations conform to the assumptions of the statistical method.

A nonidentity prior residual covariance matrix drastically alters the observation/sensitivities. The impact can be demonstrated by rewriting the right-hand side of the normal equations $J^{\mathrm{T}} C_y^{-1} y = J'^{\mathrm{T}} y'$ in terms of a modified Jacobian $J' = C_y^{-1/2} J$ and a modified residual vector $y' = C_y^{-1/2} y$. The premultiplication by the matrix square root implies that each original row is scaled by a weight of the form $\sigma^{-1}_{y_i}$. Columns of the modified Jacobian are shown in Fig. 6. The noise power parameters now exhibit a clear polynomial behavior. Reflected power remains a scaled version of the detrended SNR, although now in a logarithmic scale, which gives more weight to interference troughs than to peaks. Reflector height and phase shift sensitivities become less distinct, as the heterogeneous weights suppress the signal at high elevation angles. Unfortunately, this sensitivity conformation exacerbates the correlation between the two parameters. If one were to design an instrument, uniformly precise SNR measurements (in watts per watt units) would yield more precise reflector height estimates. One region that remains with enhanced discrimination is near the horizon, where reflector height sensitivity vanishes, while the phase-shift sensitivity does not.

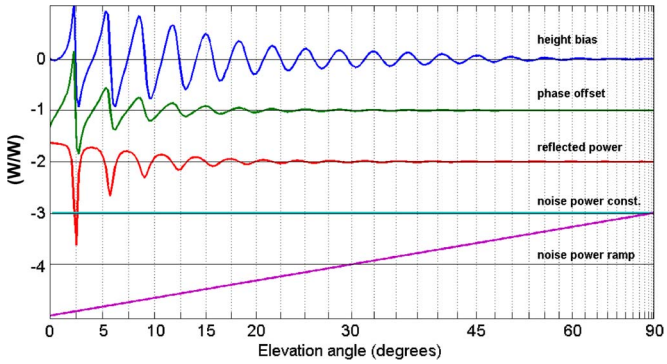

Fig. 6. Sensitivity of observations (in original units of decibels) to changes in each bias, after accounting for the varying observation uncertainty; curves are scaled and displaced vertically (1.0 W/W) for clarity.

To make it safer to neglect correlations, we decimated samples regularly spaced in sine of elevation angle (with eventual gaps). This is preferable to measurements regularly spaced in time, which translates into a sparser and denser sampling, respectively, near the horizon and zenith, as satellites appear to stall momentarily at their culmination point. Left alone, this would skew the inversion toward the more numerous samples.

V. Performance Simulations

In this section, we use simulations to assess the performance of the inversion procedure, in terms of the parameter errors and how well they are bounded by the expected parameter uncertainty.

A. Uncertainty Quantification

The (unscaled) parameter posterior covariance matrix

$$C_{\widehat{x}} = \left(J^{\mathrm{T}} C_y^{-1} J\right)^{-1} \tag{32}$$

is involved in the computation of $\widehat{x}$ itself (28) and depends only on the prior specification of the functional and stochastic models, independently from the actual measurements Y. However, the parameter posterior standard deviation vector $\Sigma_{\widehat{x}} = \sqrt{\mathrm{diag}(C_{\widehat{x}})}$, e.g., $\sigma_{\widehat{H}_B} = \Sigma_{\widehat{x}}(1)$, depends on the values of the parameters. For example, smaller reflection power results in more uncertain reflector height estimates as a consequence of vanishing interference fringes. Diminishing reflector heights are also more uncertain, as the reflector height sensitivity curve becomes confounded with, less distinct from, that of all other parameters; furthermore, fewer oscillation cycles are included in a track, from horizon to zenith.

The uncertainty of parameters depends on the parameter values themselves. For example, in Fig. 7, we plot the reflector height uncertainty $\sigma_{\widehat{H}_B}$ versus total reflector height $H = H_A - H_B$. Smaller reflector heights produce more uncertain reflector

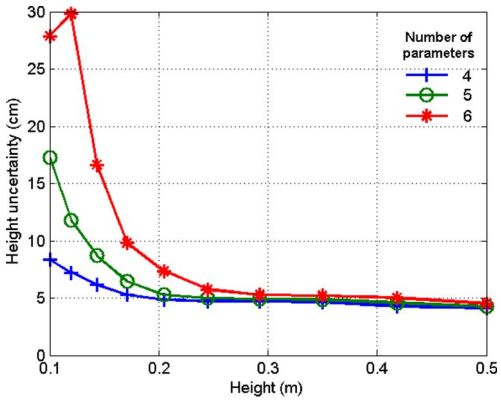

Fig. 7. Reflector height uncertainty versus total reflector height, for increasing number of parameters (equivalent to the detrending polynomial degree plus three fixed parameters).

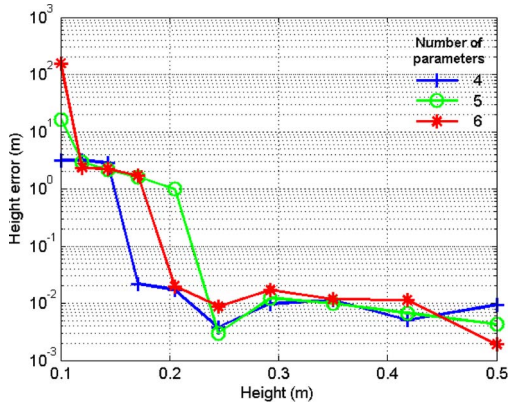

Fig. 8. Reflector height error (estimated minus true) versus true reflector height, for increasing number of parameters (equivalent to the detrending polynomial degree plus three fixed parameters).

height estimates. This is a direct consequence of the reflector height sensitivity curve becoming less distinct from the other parameters, which is more so as additional parameters are estimated and as fewer oscillation cycles are sampled in a track. This will be discussed further in the next section.

We multiply the parameter uncertainties, e.g., $\widehat{\sigma}_{\widehat{H}_B} = \widehat{\sigma}_0 \sigma_{\widehat{H}_B}$, by the scaled root-mean-square error (rmse) $\widehat{\sigma}_0 = \sqrt{\mathrm{SSR}/v}$, where $\mathrm{SSR} = y^{\mathrm{T}} C_y^{-1} y$ is the (weighted) sum of squared residuals and $v \approx m - n$ is the statistical degree of freedom (for m elements in the observation vector Y and n elements in the parameter vector X). If functional and stochastic models have been fully specified, $\widehat{\sigma}_0^2$ will be close to unity, making this scaling moot. More generally, though, its exact value is not known *a priori* and should be estimated as in terms of SSR. This factor contributes to a more realistic parameter uncertainty quantification. It accounts not only for the measurement noise but also for imperfections in the forward model–any mismatch between measurement and simulation will lead to an inflated $\widehat{\sigma}_0^2$.

B. Inversion Errors

Inversion errors are the discrepancy between retrieved inversion estimates and their true values, where the latter is known in simulations. Here, we focus on the reflector height retrieval because it is most relevant to estimation of snow depth. Its error depends primarily on reflector height itself (Fig. 8). The inversion performance deteriorates with decreasing reflector height, as trend and fringes become confounded, with the low-frequency interference fringe resembling a low-order polynomial. Notice that, for a fixed *a priori* height H_A, a smaller total reflector height $H = H_A - H_B$ corresponds to larger unknown height biases H_B, e.g., as when the snow accumulates up to the antenna level.

A second factor contributing to reflector height errors is the polynomial degree adopted for the noise power bias K used in the preliminary detrending of observations or, equivalently, the total number of parameters p—which includes reflector height, phase shift, and reflection power bias [see (25)]. Normally, we estimate only constant $K_{\mathrm{dB}}^{(0)}$ (a total of four parameters; $p = 4$) and linear $K_{\mathrm{dB}}^{(1)}$ terms ($p = 5$), which serve to scale the nonlinear trend tSNR provided by the forward model. If we could not rely on the aid offered by the forward model and had to detrend observations using solely a higher order polynomial, this empirical trend could inadvertently take away part of the fringes. Indeed, estimating a quadratic coefficient $K_{\mathrm{dB}}^{(2)} (p = 6)$ causes the reflector height error to increase significantly at small heights. For larger reflector height values, detrending is not a challenge. In this case, the nonlinear problem is well approximated by a linear expansion, and the observation/parameter sensitivities yield realistic uncertainties vis-à-vis parameter errors as well as their observability.

Inversion error also depends on the reflection power bias. It again exacerbates the possibility for confusion between the trend and the fringes. This is true even assuming noise-free measurements. Random noise further amplifies the reflection power bias effect, as small-amplitude fringes are more easily destroyed; even large-height fringes can then be disturbed. We have assumed tracks spanning the full range from horizon to zenith; satellites culminating low in the sky yield more challenging shorter tracks. Throughout, we have used a fixed 2-m initial reflector height guess (even for smaller reflector heights); a better guess would undoubtedly decrease errors, but it is impractical beyond simulations. We averaged out the dependence on reflection phase shift. In this case, the mean error loses relevance as a near-zero net value might include large positive and negative values; rms is a more representative statistic.

VI. Directional Dependence

A. Observation Importance

It is important to know which observations contribute the most information. One way of quantifying this is in terms of the impact of each observation on the parameter uncertainty. If we were estimating reflector height only, the observation importance would be proportional to the respective observation-parameter sensitivity squared. In reality, the information contributed by each observation is not used solely to determine reflector height, rather is dispersed among all parameters. To generalize the notion that the presence of observations at certain locations is inconsequential while the absence of others

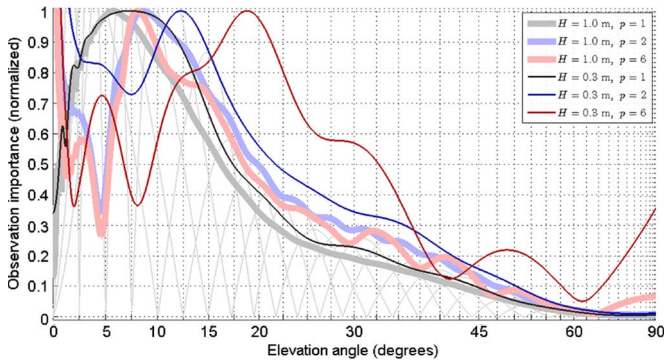

Fig. 9. Observation importance in determining reflector height under different conditions: total reflector height (H value) and number of simultaneous parameters (p value: 1 indicates reflector height only, 2 indicates reflector height and phase shift, and 6 includes additionally a scalar reflection power bias and three polynomial coefficients for direct power bias).

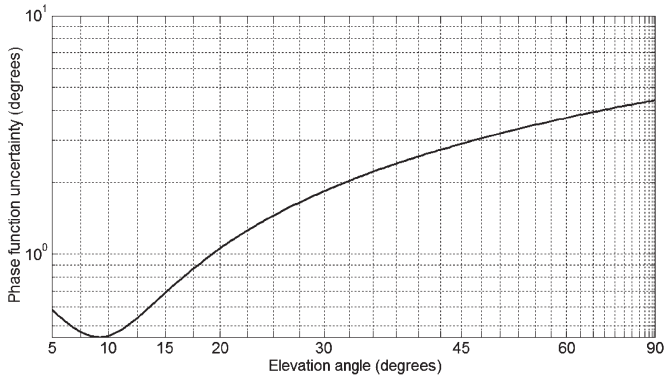

Fig. 10. Uncertainty of full phase function, propagated from the uncertainty of reflector height and of phase shift as well as their correlation.

would be crucial, we look at the reflector height posterior uncertainty.

The original uncertainty value $\widehat{\sigma}_{\widehat{H}}$ (we drop the subscript B for brevity) is obtained by retaining all observations. We withdraw (with replacement) each ith observation of the total of n observations by removing (one at a time) the corresponding row $J(i,:)$ from the modified Jacobian matrix J

$$J_i = \begin{bmatrix} J(1:i-1,:) \\ J(i+1:n,:) \end{bmatrix}. \tag{33}$$

We utilize this new Jacobian J_i to obtain the respective leave-one-out covariance matrix $C_{i\widehat{x}} = (J_i^{\mathrm{T}} J_i)^{-1}$. The observation importance is calculated as the relative increase in uncertainty between new $\sigma^2_{i\widehat{H}} = C_{i\widehat{x}}(1,1)$ and original $\sigma^2_{\widehat{H}}$ values

$$\Delta\sigma^2_{i\widehat{H}} = \left(\sigma^2_{i\widehat{H}} - \sigma^2_{\widehat{H}}\right)/\sigma^2_{\widehat{H}}. \tag{34}$$

Finally, we report the mean importance

$$\Delta\overline{\sigma}^2_{i\widehat{H}} \approx 4^{-1} \sum_{k=1}^{4} \Delta\sigma^2_{i\widehat{H}}\Big|_{\varphi_B(k)} \tag{35}$$

where the averaging takes place over a regularly spaced phase-shift domain $\varphi_B = [0, 90°, 180°, 270°]$.

Fig. 9 shows as a smooth thick gray line the mean importance when estimating reflector height only (number of parameters $p = 1$). The contributing phase-dependent individual importances are shown as thin gray lines in the background. The former is essentially the envelope of the latter ones. A thick blue line is used to represent the observation importance in determining reflector height when a phase shift is also estimated $\Delta\overline{\sigma}^2_{i\widehat{H}}|^{p=2}$ (two simultaneous parameters; $p = 2$). Notice that the curve has shifted to the right compared to when estimating a single parameter $(p = 1)$, $\Delta\overline{\sigma}^2_{i\widehat{H}}|^{p=1}$; observations at higher elevation angles become more important. Also, the near-horizon region gains in importance; this is a manifestation of the enhanced discrimination, between reflector height and phase-shift sensitivities, as discussed for Fig. 5. When the number of simultaneous parameters is raised closer to the level used in practice, with six parameters $(p = 6)$, $\Delta\overline{\sigma}^2_{i\widehat{H}}|^{p=6}$, the observation importance becomes more detailed (light-red thick curve), although the overall shape follows the previous one (light-blue thick curve), $\Delta\overline{\sigma}^2_{i\widehat{H}}|^{p=2}$.

B. Parameter Reach

A related question is at what elevation angles the parameter estimates are best determined. Here, we focus on the phase parameters instead of reflection power or noise power parameters.

We can utilize the estimated reflector height $\widehat{H}_B$ and phase shift $\widehat{\varphi}_B$ to evaluate the full phase bias function $\widehat{\phi}_B = \widehat{\varphi}_B + 4\pi\lambda^{-1}\widehat{H}_B \sin e$ over varying elevation angles e. Similarly, we can extract the corresponding 2-by-2 portion of the parameter posterior covariance matrix $\widehat{C}_{\widehat{x}}$, containing the uncertainty for reflector height $\widehat{\sigma}_{\widehat{H}_B}$ and for phase shift $\widehat{\sigma}_{\widehat{\varphi}_B}$, as well as their correlation ρ

$$\begin{bmatrix} \widehat{\sigma}^2_{\widehat{H}_B} & \rho\,\widehat{\sigma}_{\widehat{H}_B}\widehat{\sigma}_{\widehat{\varphi}_B} \\ \rho\,\widehat{\sigma}_{\widehat{H}_B}\widehat{\sigma}_{\widehat{\varphi}_B} & \widehat{\sigma}^2_{\widehat{\varphi}_B} \end{bmatrix} \tag{36}$$

which is then propagated to obtain the full phase uncertainty $\widehat{\sigma}_{\widehat{\phi}_B}$ (see Fig. 10).

The uncertainty $\widehat{\sigma}_{\widehat{\phi}_B}$ attains a clear minimum versus elevation angle. The least-uncertainty elevation angle $e_p = \arg\min(\widehat{\sigma}_{\widehat{\phi}_B})$ can be found in the roots of the derivative $\partial\widehat{\sigma}_{\widehat{\phi}_B}/\partial e_p = 0$, whose solution reads

$$4\pi\lambda^{-1}\sin e_p = -\frac{\widehat{\sigma}_{\widehat{H}_B} + \widehat{\sigma}_{\widehat{\phi}_B}}{2\rho\widehat{\sigma}_{\widehat{H}_B}}. \tag{37}$$

We will call $e_p(\sim 10°)$ peak elevation angle as it pinpoints the observation direction where reflector height and phase shift have the least uncertainty or are best determined (in combined form and not individually). The azimuth and epoch coinciding with the peak elevation angle act as track tags, later used for clustering similar tracks and analyzing their time series of retrievals.

Finally, if we normalize phase uncertainty by its value at the peak elevation angle $\widehat{\sigma}_{\widehat{\phi}_B}(e)/\widehat{\sigma}_{\widehat{\phi}_B}(e_p)$ and then plot such sensing weights (between 0 and 1) versus the radial or horizontal distance to the center of the first Fresnel zone [12] at each elevation angle, we obtain Fig. 11. It can be interpreted as the reflection footprint, indicating the importance of varying distances, with a longer far tail and a shorter near tail (respectively, regions beyond and closer than the peak distance). The implications for *in situ* data collection are clear: One

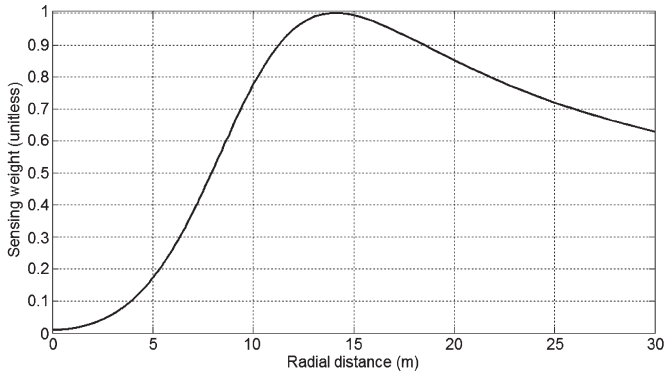

Fig. 11. Reflection footprint in terms of a sensing weight (between 0 and 1) defined as the normalized reciprocal of full phase uncertainty, plotted versus the radial or horizontal distance from the receiving antenna to the center of the first Fresnel zone at each elevation angle; valid for an upright 2-m tall antenna; the receiving antenna is at zero radial distance.

should sample more intensely near the peak distance ($\sim$15 m) and less so in the immediate vicinity of the GPS, tapering it off gradually away from the GPS. As a caveat, these conclusions are not necessarily valid for antenna setups other than the one considered here, e.g., tipped instead of upright antenna, or installations at values much larger or smaller than the reflector height assumption used here ($\sim$2 m).

VII. Conclusion

We have formulated a forward/inverse approach for the estimation of snow depth from GPS SNR observations. We have used simulations to illustrate various aspects of the model, such as trend and fringes, sensitivity of observations to parameter changes, parameter space in which the objective function is embedded (including the indeterminacy of reflector heights under small reflection amplitude conditions), and expected reflector height inversion error and how well it was bounded by the model uncertainty. In part II, we will validate the retrieval algorithm by comparison to *in situ* data collected at three different GPS locations over a multiyear period. Future work could assess the various effects currently neglected [19, chap. 6], not only in terms of the impact on forward modeled observations but, more importantly, the feasibility of having separate inverse parameter retrievals or at least to what extent their neglect would cause a bias in reflector height and snow depth.

References

[1] R. L. Armstrong and E. Brun, Eds., *Snow and Climate—Physical Processes, Surface Energy Exchange and Modeling*. Cambridge, U.K.: Cambridge Univ. Press, 2008.

[2] T. P. Barnett, J. C. Adam, and D. P. Lettenmaier, "Potential impacts of a warming climate on water availability in snow-dominated regions," *Nature*, vol. 438, no. 7066, pp. 303–309, Nov. 2005.

[3] H. Rott, S. H. Yueh, D. W. Cline, C. Duguay, R. Essery, C. Haas, F. Hélière, M. Kern, G. Macelloni, E. Malnes, T. Nagler, J. Pulliainen, H. Rebhan, and A. Thompson, "Cold Regions Hydrology High-Resolution Observatory for Snow and Cold Land Processes," *Proc. IEEE*, vol. 98, no. 5, pp. 752–765, May 2010.

[4] M. D. Jacobson, "Dielectric-covered ground reflectors in GPS multipath reception–Theory and measurement," *IEEE Geosci. Remote Sens. Lett.*, vol. 5, no. 3, pp. 396–399, Jul. 2008.

[5] M. D. Jacobson, "Inferring snow water equivalent for a snow-covered ground reflector using GPS multipath signals," *Remote Sens.*, vol. 2, no. 10, pp. 2426–2441, Oct. 2010.

[6] E. Cardellach, F. Fabra, A. Rius, S. Pettinato, and S. D'Addio, "Characterization of dry-snow sub-structure using GNSS reflected signals," *Remote Sens. Environ.*, vol. 124, pp. 122–134, Sep. 2012.

[7] N. Rodriguez-Alvarez, A. Aguasca, E. Valencia, X. Bosch-Lluis, A. Camps, I. Ramos-Perez, H. Park, and M. Vall-llossera, "Snow thickness monitoring using GNSS measurements," *IEEE Geosci. Remote Sens. Lett.*, vol. 9, no. 6, pp. 1109–1113, Nov. 2012.

[8] M. Ozeki and K. Heki, "GPS snow depth meter with geometry-free linear combinations of carrier phases," *J. Geod.*, vol. 86, no. 3, pp. 209–219, Mar. 2012.

[9] N. Najibi and S. Jin, "Physical reflectivity and polarization characteristics for snow and ice-covered surfaces interacting with GPS signals," *Remote Sens.*, vol. 5, no. 8, pp. 4006–4030, Aug. 2013.

[10] K. M. Larson, E. D. Gutmann, V. U. Zavorotny, J. J. Braun, M. W. Williams, and F. G. Nievinski, "Can we measure snow depth with GPS receivers?" *Geophys. Res. Lett.*, vol. 36, no. 17, pp. L17502-1–L17502-5, Sep. 2009.

[11] E. D. Gutmann, K. M. Larson, M. W. Williams, F. G. Nievinski, and V. Zavorotny, "Snow measurement by GPS interferometric reflectometry: An evaluation at Niwot Ridge, Colorado," *Hydrol. Process.*, vol. 26, no. 19, pp. 2951–2961, Sep. 2012.

[12] K. M. Larson and F. G. Nievinski, "GPS snow sensing: Results from the EarthScope Plate Boundary Observatory," *GPS Solutions*, vol. 17, no. 1, pp. 41–52, Jan. 2013.

[13] F. G. Nievinski and K. M. Larson, "Inverse modeling of GPS multipath for snow depth estimation—Part II: Application and validation," *IEEE Trans. Geosci. Remote Sens.*, vol. 52, no. 10, pp. 6564–6573, Oct. 2014.

[14] F. G. Nievinski and K. M. Larson, "Forward modeling of GPS multipath for near-surface reflectometry and positioning applications," *GPS Solutions*, pp. 1–14, 2013.

[15] P. Beckmann and A. Spizzichino, *The Scattering of Electromagnetic Waves from Rough Surfaces*. New York, NY, USA: Pergamon, 1963.

[16] P. Beckmann and A. Spizzichino, *The Scattering of Electromagnetic Waves from Rough Surfaces*. Norwood, MA, USA: Artech House, 1987.

[17] M. Tiuri, A. Sihvola, E. Nyfors, and M. Hallikaiken, "The complex dielectric constant of snow at microwave frequencies," *IEEE J. Ocean. Eng.*, vol. 9, no. 5, pp. 377–382, Dec. 1984.

[18] Y. Georgiadou and A. Kleusberg, "On carrier signal multipath effects in relative GPS positioning," *Manuscripta Geod.*, vol. 13, no. 3, pp. 172–179, 1988.

[19] F. G. Nievinski, "Forward and inverse modeling of GPS multipath for snow monitoring," Ph.D. dissertation, Univ. Colorado Boulder, Boulder, CO, USA, 2013.

[20] R. L. Armstrong, M. J. Brodzik, K. Knowles, and M. Savoie, Global Monthly EASE-Grid Snow Water Equivalent Climatology 2005. [Online]. Available: http://nsidc.org/data/nsidc-0271.html

Felipe G. Nievinski received the B.E. degree in geomatics from Universidade Federal do Rio Grande do Sul (UFRGS), Porto Alegre, Brazil, in 2005, the M.Sc.E. degree in geodesy from the University of New Brunswick, Fredericton, NB, Canada, in 2009, and the Ph.D. degree in aerospace engineering sciences from the University of Colorado Boulder, Boulder, CO, USA, in 2013.

He is a Postdoctoral Researcher with Universidade Estadual Paulista Júlio de Mesquita Filho (UNESP), Presidente Prudente, Brazil, where he works in the field of GPS multipath reflectometry.

Kristine M. Larson received the B.A. degree in engineering sciences from Harvard University, Cambridge, MA, USA, in 1985 and the Ph.D. degree in geophysics from the Scripps Institution of Oceanography, University of California at San Diego, La Jolla, CA, USA, in 1990.

She is a professor of aerospace engineering sciences with the University of Colorado Boulder, Boulder, CO, USA. Her current research focuses on GPS reflections.